



Crack identification using electrical impedance tomography and transfer learning

Said Quqa^{1,2,3} | Luca Landi¹ | Kenneth J. Loh^{2,3}

¹Department of Civil, Chemical, Environmental and Materials Engineering, University of Bologna, Bologna, Italy

²Department of Structural Engineering, University of California San Diego, La Jolla, California, USA

³Active, Responsive, Multifunctional, and Ordered-materials Research (ARMOR) Laboratory, University of California San Diego, La Jolla, California, USA

Correspondence

Said Quqa, Department of Civil, Chemical, Environmental and Materials Engineering, University of Bologna, Viale del Risorgimento 2, 40136 Bologna, Italy.
Email: said.quqa2@unibo.it

Kenneth J. Loh, Department of Structural Engineering, University of California San Diego, 9500 Gilman Dr MC 0085, La Jolla, CA 92093-0085, USA.
Email: kenloh@ucsd.edu

Funding information

Cooperative Research Agreements, Grant/Award Numbers: W912HZ-17-2-0024, W9132T-22-2-20014; European Union's Horizon 2020, Grant/Award Number: 777822

Abstract

Sensing skins and electrical impedance tomography constitute a convenient and inexpensive alternative to dense sensor networks for distributed sensing in civil structures. However, their performance can deteriorate with the aging of the sensing film. Guaranteeing high identification performance after minor lesions is crucial to improving their ability to identify structural damage. In this paper, electrical resistance tomography is used to identify the crack locations in nanocomposite paint sprayed onto structural components. The main novelty consists of using crack annotations collected during visual inspections to improve the crack identification performance of deep neural networks trained using simulated datasets through transfer learning. Transfer component analysis is employed for simulation-to-real information transfer and applied at a population level, extracting low-dimensional domain-invariant features shared by simulated models and structures with similar geometry. The results show that the proposed method outperforms traditional approaches for crack localization in complex damage patterns.

1 | INTRODUCTION

Machine learning has been widely employed in the last decades for structural health monitoring (SHM) in civil engineering to improve the performance, accuracy, and user-friendliness of damage identification methods. The integration of signal processing techniques and machine learning allowed for extracting hidden features from the structural responses and automatically estimating the global state of the monitored structure (Rafiei & Adeli, 2017). Research has also been conducted to propose ready-to-use general identification frameworks

(Soleimani-Babakamali et al., 2022). While automatic assessment of the state of a structure may be helpful for large-scale monitoring (e.g., many bridges in a region), widespread adoption of fully automated procedures is still limited in practice by the lack of familiarity and trust of professionals. Indeed, visual inspections are still the most widespread methods to assess the health state of structural components (Nayyeri et al., 2019). Also, local inspections are necessary to identify particular damage types. For most structures, superficial cracks are the first sign of damage (C. Zhang et al., 2020), which may manifest due to the exceedance of a limit surface tension or fatigue

This is an open access article under the terms of the [Creative Commons Attribution](https://creativecommons.org/licenses/by/4.0/) License, which permits use, distribution and reproduction in any medium, provided the original work is properly cited.

© 2023 The Authors. *Computer-Aided Civil and Infrastructure Engineering* published by Wiley Periodicals LLC on behalf of Editor.



without impacting the global dynamic behavior of the system substantially.

In this context, vision-based algorithms have proven extremely valuable in supporting operators with objective analyses (Deng et al., 2020; Liu et al., 2020). For instance, Chun et al. (2022) developed a deep learning-based method to describe the damage condition of a bridge through text explanation. Y. Pan and Zhang (2022) proposed a dual attention deep neural network (DNN) to classify damage in steel elements automatically and depict their shapes on the structure. Zheng et al. (2022) proposed a multistage semi-supervised active learning framework to measure the width of cracks in bridges quickly and reliably. The high dimensionality of the input features in vision-based methods (i.e., pixels) typically leads to relatively high computational runtime. Although research efforts have been devoted to improving the training efficiency of vision-based methods for crack identification (Y. Zhang & Yuen, 2021), other aspects make vision-based methods not always applicable for permanent SHM, such as interfering objects and varying lighting conditions.

Alternatively, self-sensing materials can be coupled with methods to identify the bulk conductivity variation of structural elements or imaging techniques. Conductivity is related to the mechanical properties of the interrogated body, and its discontinuities (e.g., cracks) generate conductivity alterations that can be detected and localized. Advantages of self-sensing materials include high sensitivity to disconnections and altered strain states (enabled by electron tunneling; Hu et al., 2008; Tallman et al., 2014) and ease of interrogation without external instruments.

Electrical impedance tomography (EIT) is an imaging method (Borcea, 2002; Capps & Mueller, 2020; Holder, 2004; Z. Lin et al., 2020) recently used for nondestructive evaluation and SHM (Loh et al., 2009; Tallman & Smyl, 2020) to infer a dense distribution of conductivity properties of a body interrogated electrically from sparse voltage measurements. While piezoresistive structural components can only be used for newly built structures or replacements (Meoni et al., 2020), functional coatings can be applied to regular structural elements to enable the self-sensing capability of the outer surface (Jauhiainen et al., 2021). In this context, Hou et al. (2007) first proposed a multifunctional carbon nanotube-based thin film to localize conductivity variations due to mechanical phenomena and chemical agents using an EIT-based method. In the same year, Loh et al. (2007) presented a carbon nanotube-polyelectrolyte functional film deposited layer-by-layer to encode multiple transduction mechanisms for corrosion and strain sensing. A few years later, Loh et al. (2009) applied carbon nanotube-polymer thin films to aluminum plates for impact damage localization. Loyola et al. (2010) studied the bulk resistivity and inter-nanotube electrical behavior of piezoresistive thin films based on carbon nan-

otubes deposited onto glass fiber structures to identify the strain state and microcracking of the substrate. Some authors used different paint formulations based on silver (Seppänen et al., 2017) and copper (Hallaji et al., 2014) to identify cracks and corrosion. Moreover, other scholars (Gupta et al., 2020; Sijia Li et al., 2022; Y. A. Lin et al., 2021) identified strain in different directions using a patterned sensing film through a difference imaging approach (i.e., using the difference of voltage measurements collected at different times to reconstruct the conductivity variation instead of the absolute conductivity of the inspected body).

Due to the ill-posedness of the conductivity reconstruction problem through EIT, extensive research has been conducted to formulate effective mathematical resolution strategies. The most popular ones involve the recursive resolution of a weak formulation of Kirchoff's law until the solution matches the measurements (Gupta et al., 2017) or the direct inversion of a strongly ill-conditioned problem (Gupta et al., 2020). In general, both methods also need regularization techniques. Absolute imaging approaches typically showed higher resolution in reconstructed images when observation noise and modeling errors are limited, compared to difference imaging methods (Hallaji & Pour-Ghaz, 2014; Hallaji et al., 2014). On the other hand, difference imaging is generally less sensitive to error sources, but it may suffer from reconstruction "artifacts," especially in the regions close to the electrodes (Hallaji & Pour-Ghaz, 2014).

As an alternative to physical-based algorithms, machine learning approaches have recently gained popularity for EIT imaging. Z. Lin et al. (2020) found that approaches entirely based on neural networks may be faster than physical-based procedures but generally provide less robust results. Z. Chen et al. (2021) used a convolutional neural network coupled with group sparsity regularization to improve reconstruction quality. Very recently, Jeon et al. (2022) employed a deep learning-based approach to identify rebar position in reinforced concrete elements with high accuracy using a frequency-difference EIT approach. L. Chen, Hassan, et al. (2022) employed a deep learned framework to reconstruct the strain and stress fields in piezoresistive nanocomposites for damage identification, bypassing the resolution of the inverse EIT problem. In this case, the authors used an absolute imaging approach due to its suitability for reducing the discrepancy between simulated data (used for training) and real measurements. Xue and Zhang (2022) used a dual-channel inception-densebam network model integrated with an attention mechanism for damage detection in carbon fiber-reinforced polymers in a difference imaging approach, which proved particularly robust to noise.

A well-known issue affecting supervised machine learning approaches is that large datasets representative of realistic damaged conditions (typically missing for



practical applications) must be used for training. Transfer learning was proposed to “transfer” information between two domains with common characteristics (i.e., a source and a target domain) to extend the knowledge on the target domain, for which fewer observations are typically available. In the field of crack identification, C. Zhang et al. (2020), Shengyuan Li et al. (2019), and Wu et al. (2021) used transfer learning to improve the performance of neural networks for vision-based damage identification by retraining pre-trained networks. These approaches are typically known as “parameter-level” methods or “fine-tuning” of pre-trained models and do not modify the features.

As datasets are typically rare for real damaged structures, few instances collected for real cracks may be insufficient for information transfer in parameter-level approaches. In these cases, valuable information can be transferred from simulated models to the real-world domain. This field is typically known as “sim-to-real” transfer. However, synthetic and real features may substantially differ due to noise and slight differences in geometry or materials between simulated models and real structures. In this context, domain-invariant features can be obtained through feature-level transfer learning, also known as “domain adaptation” techniques (Y. Lin et al., 2022; S. J. Pan et al., 2011). This concept can also be applied among a population of structures, where some features are shared by different individuals with common characteristics, in a population-level analysis (Bull et al., 2021). This allows for improving the knowledge of specific structures for which sufficiently large datasets are missing.

Previous studies showed that, in some cases, synthetic data alone could be enough to train neural networks for the identification of conductivity changes due to damage or strain variations when the sensing body is originally undamaged (Quqa et al., 2022). Nevertheless, while early damage might be identified with good accuracy (Quqa et al., 2023), the performance of neural networks typically degrades with damage severity (L. Chen, Gallet, et al., 2022; Hallaji et al., 2014; Seppänen et al., 2017). However, not all surface disconnections are necessarily related to structural damage. External agents may damage the

sensing films, thus reducing their ability to identify future damage. Extending the lifespan of sensing films for SHM is critical to reducing replacement costs and improving identification performance when the sensing material is already damaged.

This study proposes a new approach based on transfer learning to gather information observed in the real environment through visual inspections conducted after detecting early damage and exploit it to update a DNN trained with synthetic data (i.e., generated by a finite element [FE] model). The main goal of this method is to improve the capability to detect progressive cracks in future monitoring.

In this study, domain adaptation is applied for the first time for crack identification, transferring information from the simulated to the real domain and at a population level. Moreover, this study is the first to use a domain adaptation method to solve the EIT imaging problem.

This paper is organized as follows: Section 2 introduces the general methodology proposed. Section 3 describes the theoretical background of FE formulation for the EIT problem, which is necessary to generate the structure of the source domain. Section 4 defines the neural network architecture used for EIT imaging. Section 5 is the core of the paper and describes in detail the method proposed to transfer information from simulated data and other structures in the population to improve the performance of the neural network employed for crack identification. Section 6 describes experimental tests conducted in the laboratory and discusses the results summarized in the conclusions (Section 7).

2 | GENERAL METHODOLOGY

A scheme of the proposed approach is summarized in Figure 1. First, a FE model of the sensing film deployed on a structural component is built (see Section 3), and several damage scenarios are simulated by setting the conductivity to zero in some regions (more details are provided in the applications section). A preliminary DNN is then trained

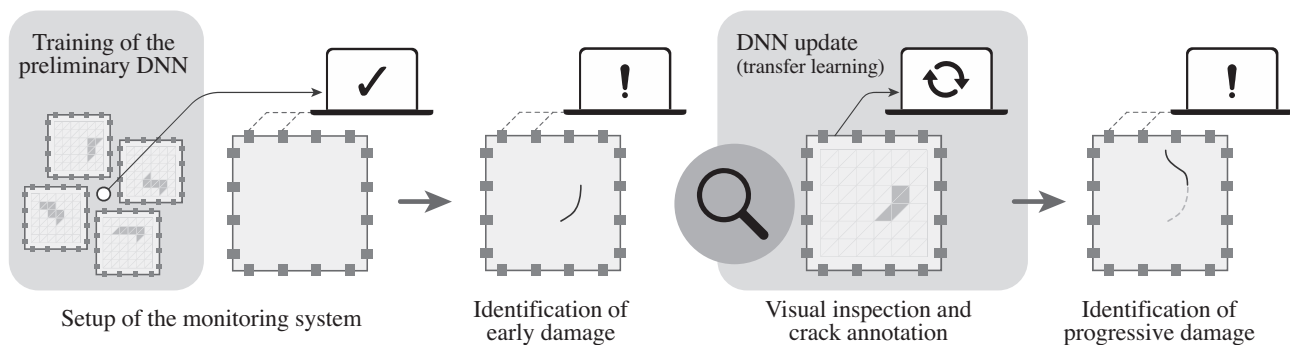


FIGURE 1 Scheme of the proposed approach. DNN, deep neural network.



using simulated data alone (see Section 4), and an SHM system is deployed to identify early cracks from EIT data based on this DNN (left-hand part of Figure 1). Literature studies showed that DNNs could be successfully employed for this task (L. Chen, Gallet, et al., 2022).

When early damage is detected, visual inspections are typically scheduled in usual practice (this is the typical case in which the SHM system triggers human intervention). In this phase, operators can use manual or automatic annotation tools (J. Chen et al., 2022; Liu et al., 2020), for example, by means of unmanned inspection devices, to generate damage labels associated with the input dataset used to predict the anomaly (central part of Figure 1).

After that, if inspectors decide that the structure can still be used, the sensing film should still be able to identify further damage with the same accuracy as before. Therefore, this study proposes a procedure to update the preliminary DNN by including the real measurement and the damage label annotated during the visual inspection in the training process to improve the reconstruction performance in the following monitoring phases. This process is carried out at the feature level, using the transfer component analysis (TCA; S. J. Pan et al., 2011), a semi-supervised domain adaptation technique, to account for the inherent differences between simulated and real data (see Section 5). Specifically, instead of using raw voltage measurements, the updated DNN is trained using domain-invariant features obtained through TCA.

This method can also be applied at a population level, such that different sensing films with the same geometry can benefit from data collected in early damage states from a given individual.

3 | FE FORMULATION

EIT was first used as a noninvasive technique of medical imaging in which the electrical impedance of a conductive body is inferred from sparse electrode measurements on its boundary to form a tomographic image of the body itself. This problem, also known as the “inverse” EIT problem, was initially formulated by Calderón (2006). Analytically, it consists of recovering a distribution of the conductivity σ of a body Ω from the relation that exists between the potential on its boundary $\phi|_{\Gamma}$ (where Γ is the boundary of Ω) with the current density j (Holder, 2004). This relation can be either expressed as the “Dirichlet to Neuman” (DtN) map $\Lambda_{\sigma} : \phi|_{\Gamma} \rightarrow j$, or the “Neuman to Dirichlet” map $\Lambda_{\sigma}^{-1} : j \rightarrow \phi|_{\Gamma}$. The inverse EIT problem has generally been studied using a discrete approximation through finite FE modeling for practical applications. Typically, the complete electrode model (CEM; Holder, 2004) is employed to incorporate the proper boundary conditions to model

the shunting effect and account for the contact impedance of the electrodes with sufficient accuracy. Let a current I_q be applied to the conductive body using Q electrodes with areas E_q ($q = 1, \dots, Q$), and let Γ_1 and Γ_2 be the region of the boundary covered by the electrodes and the remaining part of the boundary, respectively. The CEM boundary conditions are defined such that

$$\int_{E_q} j dS = I_q \quad \text{on } \Gamma_1 \quad (1)$$

$$j = 0 \quad \text{on } \Gamma_2 \quad (2)$$

where dS represents a generic surface differential.

The impedance z_q at the contact region between the q th electrode and the body is accounted for through the following condition:

$$\phi + z_q j = v_q \quad (3)$$

where ϕ is the potential in the body, and v_q is the relevant voltage measurement with respect to some arbitrary reference.

If the injected current is direct (DC), the EIT specializes in electrical resistance tomography (ERT). In this context, the DtN map can be written as

$$\mathbf{i}_q = \mathbf{Y} \mathbf{v}_q \quad (4)$$

where $\mathbf{i}_q \in \mathbb{R}^Q$ and $\mathbf{v}_q \in \mathbb{R}^Q$ are vectors representing a current injection and a related voltage measurement (between pairs of electrodes) on the boundary of the interrogated body, while $\mathbf{Y} \in \mathbb{R}^{Q \times Q}$ is the transfer conductance matrix. In general, different instances of \mathbf{i}_q and the associated \mathbf{v}_q are necessary to map the entire matrix \mathbf{Y} , which are generally selected according to specific measurement protocols designed to minimize the number of interrogations. For instance, the adjacent (or Sheffield—Loyola et al., 2013) interrogation pattern consists of injecting the current into couples of adjacent electrodes, one couple at a time. The boundary voltage measured between all the other adjacent electrode couples is recorded simultaneously, and the process is repeated until the current is injected into all the electrodes.

In the discrete formulation, the inverse ERT problem consists of recovering a conductivity vector $\sigma \in \mathbb{R}^M$ from \mathbf{Y} , with M denoting the number of triangular discrete elements considered in the description of the conductive body.

A weak form of the EIT problem can be formulated to obtain a solution only at the N mesh nodes of the FE model. The obtained results can then be interpolated over the entire region using linear shape functions w_n , with $n = 1, \dots, N$, so that a discrete approximation of the potential



can be written as

$$\phi_{FE} = \sum_{n=1}^N \phi_n w_n \quad (5)$$

The FE formulation of EIT can thus be written in a matrix form as follows:

$$\begin{bmatrix} \mathbf{0} \\ \mathbf{i} \end{bmatrix} = \begin{bmatrix} \mathbf{A}_M + \mathbf{A}_Z & \mathbf{A}_W \\ \mathbf{A}_W^T & \mathbf{A}_D \end{bmatrix} \begin{bmatrix} \phi \\ \mathbf{v} \end{bmatrix} \quad (6)$$

Here, $\phi \in \mathbb{R}^N$ and $\mathbf{v} \in \mathbb{R}^Q$ represent the vector of potentials in every node of the mesh and the boundary voltage at the electrodes, respectively, when the current represented by the generalized current vector $\mathbf{i} \in \mathbb{R}^Q$ is injected into the conductive body. $\mathbf{0}$ represents a vector with null elements. Besides, $\mathbf{A}_M \in \mathbb{R}^{N \times N}$, $\mathbf{A}_Z \in \mathbb{R}^{N \times N}$, $\mathbf{A}_W \in \mathbb{R}^{N \times Q}$, and $\mathbf{A}_D \in \mathbb{R}^{Q \times Q}$ form the global transfer conductance matrix and are defined as

$$[\mathbf{A}_M]_{n_1 n_2} = \int_{\Omega} \sigma \nabla w_{n_1} \cdot \nabla w_{n_2} dV \quad (7)$$

$$[\mathbf{A}_Z]_{n_1 n_2} = \sum_{q=1}^Q \frac{1}{z_q} \int w_{n_1} w_{n_2} E_q dS \quad (8)$$

$$[\mathbf{A}_W]_{nq} = -\frac{1}{z_q} \int w_n dS \quad (9)$$

$$[\mathbf{A}_D]_{qq} = \frac{|E_q|}{z_q} \quad (10)$$

where dV represents a generic volume differential, while the notation $[\mathbf{A}]_{ab}$ identifies the element on the a th row and b th column of the matrix \mathbf{A} . In Equation (10), \mathbf{A}_D is a diagonal matrix with zeros in the off-diagonal terms.

4 | DEEP LEARNING FOR DISTRIBUTED SENSING

The inverse ERT problem is generally computationally expensive, as it may require a recursive resolution of the forward problem (Gupta et al., 2017). Alternatively, one-step approaches have been applied in the last decades (Gupta et al., 2020). However, the issue of computational runtime is only partially addressed in these cases, as the minimization process involved consists of the inversion of large matrices.

In this study, the inverse ERT problem is addressed using a machine learning approach, which consists of representing the complex effect of localized conductivity variations on the electric field of a conductive body using a DNN. Specifically, this paper considers conduc-

tivity variations induced by discontinuities (i.e., cracks) in the conductive material. The problem is addressed from a difference imaging perspective, in which the input and output of the DNN employed for regression are represented by the difference between two voltage measurements obtained during different interrogations and the relevant conductivity variation in the FE model, respectively.

DNNs need a preliminary training process conducted using known input–output instances. Due to the substantial number of instances typically required to train a DNN appropriately, using real data for training is impractical, especially if generating the instance involves damaging the specimen, which represents the modeled body. Therefore, in this study, an extensive training dataset is generated by imposing different disconnection patterns in a simulated FE model (i.e., reducing to zero the conductivity of some elements of the mesh) and solving the forward problem for each case to obtain the voltage difference at the electrodes.

Let $\mathbf{Z} = \mathbf{Y}^{-1}$ be the transfer resistance matrix of the interrogated body and $\mathbf{I} = [\mathbf{i}_1, \dots, \mathbf{i}_Q]$ a matrix embedding the current injections of a Sheffield measurement protocol (Loyola et al., 2013). The corresponding set of boundary voltages can be expressed as $\mathbf{V} = \mathbf{Z}\mathbf{I}$, where $\mathbf{V} = [\mathbf{v}_1, \dots, \mathbf{v}_Q]$. Consider the vector $\mathbf{v} \in \mathbb{R}^K$ collecting the components of \mathbf{V} organized in a column, excluding the measurements taken at the electrodes employed for current injection to avoid inaccuracies related to the unknown contact impedance (Harikumar et al., 2013). In this case, $K = Q(Q - 3)$.

A set of C simulated discrete conductivity vectors $\sigma^{(c)}$ were generated by simulating random cracks in the FE model of the conductive material, with $c = 1, \dots, C$. For each instance, a vector $\mathbf{v}^{(c)}$ was obtained by solving the forward problem.

One possible strategy for distributed sensing through deep learning is to train a DNN with a training set defined as $\mathcal{T} = \{\delta\mathbf{V}, \delta\mathbf{\Sigma}\}$, where $\delta\mathbf{V} = [\delta\mathbf{v}^{(1)}, \dots, \delta\mathbf{v}^{(C)}]$ and $\delta\mathbf{\Sigma} = [\delta\sigma^{(1)}, \dots, \delta\sigma^{(C)}]$, with $\delta\mathbf{v}^{(c)} \in \mathbb{R}^K$ representing a normalized boundary voltage difference between conditions 0 (i.e., a baseline configuration) and c , defined as

$$\delta\mathbf{v}^{(c)} = \frac{\mathbf{v}^{(c)} - \mathbf{v}^{(0)}}{\hat{v}} \quad (11)$$

where \hat{v} is the maximum of the absolute values of the elements in $\mathbf{v}^{(0)}$, while $\delta\sigma^{(c)} \in \mathbb{R}^M$ is the difference between the conductivity distributions obtained in the same conditions:

$$\delta\sigma^{(c)} = \sigma^{(c)} - \sigma^{(0)} \quad (12)$$

This strategy was proposed in previous studies (Quqa et al., 2022; Quqa et al., 2023) and will be used here to represent the reference performance of a DNN-based method to solve the inverse ERT problem. This DNN will be referred

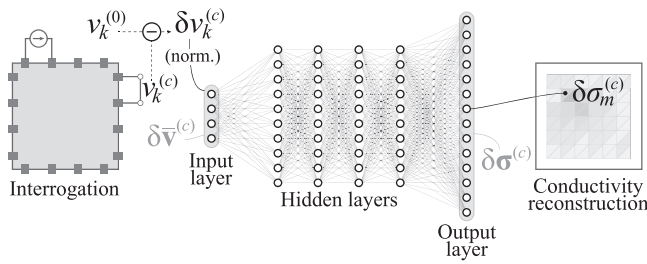


FIGURE 2 Deep neural network (DNN) architecture.

to as “preliminary” DNN hereafter, as it is trained on synthetic data alone. The architecture of the preliminary DNN used in this paper consists of an input layer of dimension K followed by four hidden layers with 2048 neurons each, activated by exponential linear unit (ELU) functions, and the output layer of dimension M , without any activation function. The choice of the number of neurons followed a trial-and-error process. The configuration used in this study provided higher identification performance using the lowest number of neurons. The ELU function was selected due to its robustness to noise, which typically leads to faster learning (Clevert et al., 2015).

Batch normalization was carried out after the input layer. A schematization of the reference DNN is reported in Figure 2.

The forward propagation in each hidden layer provides the following result:

$$\mathbf{x}_l = \text{ELU}(\mathbf{G}_l \mathbf{x}_{l-1} + \mathbf{b}_l) \quad (13)$$

where $\mathbf{G}_l \in \mathbb{R}^{R \times R}$ is the weight matrix, and $\mathbf{b}_l \in \mathbb{R}^R$ is the bias vector of the l th layer. The training process is conducted to determine the elements of the set of parameters $\mathbf{D} = \{\mathbf{G}_1, \dots, \mathbf{G}_L, \mathbf{b}_1, \dots, \mathbf{b}_L\}$ using the samples of the training dataset \mathcal{T} as follows:

$$\mathbf{D} = \arg \min_{\mathbf{D}} \left(\left\| \delta \Sigma - \delta \hat{\Sigma}(\mathbf{D}, \delta \bar{\mathbf{V}}) \right\|^2 \right) \quad (14)$$

where $\delta \hat{\Sigma}(\mathbf{D})$ is a set that includes the outputs of the DNN obtained by using all the samples in \mathcal{T} . The trained network can be used to predict the conductivity variation $\delta \hat{\sigma}^{(c)}$ associated with a measured voltage difference $\delta \bar{\mathbf{v}}^{(c)}$ at the electrode locations by feeding the DNN with $\delta \bar{\mathbf{v}}^{(c)}$ and calculating the forward propagation, up to the output layer, using the trained parameters in \mathbf{D} .

5 | INFORMATION TRANSFER

Recently published works focused on machine learning implementations to solve the inverse EIT problem,

providing promising results (L. Chen, Gallet, et al., 2022). However, due to the inherent differences between the FE model and the real body used in a field application (e.g., measurement noise, modeling, and fabrication errors), the real and virtual voltage measurements may differ substantially. In some examples, pre-processing was performed on simulated data to limit this issue (L. Chen, Hassan, et al., 2022). Yet, this approach may be challenging to apply with difference imaging.

The preliminary DNN may be the only tool available at the beginning of the monitoring process due to the lack of real datasets from the damaged structure. However, due to modeling errors, the preliminary DNN can lead to inaccurate crack localization for complex crack patterns, that is, when the sensing film is already damaged.

This paper proposes using the TCA as a pre-processing operation to extract meaningful features from simulated voltage difference datasets that overlap those extracted from real measurements collected after early damage. The extracted domain-invariant features are then used as the input to train an “updated” DNN, together with the reference conductivity distributions associated with simulated cracks, which are at the output of the DNN. The updated DNN can thus replace the preliminary DNN to predict conductivity distributions from field voltage measurements collected in the future.

To date, management decisions for damaged structures are still made upon visual inspections, which may however be triggered—and thus optimized—by automatic damage identification procedures. Suppose that a first crack is identified in the monitored structural portion by processing a voltage measurement $\delta \bar{\mathbf{v}}^{(c_r)}$. A visual inspection is thus scheduled to assess the severity of damage and take suitable action. During the inspection, the crack location can be annotated to generate a vector $\sigma^{(c_r)}$ on the mesh of the FE model by setting the conductivity of the triangular elements overlapping the actual crack to zero. This vector can then be used to generate a conductivity variation label $\delta \sigma^{(c_r)}$ with respect to a baseline condition $\sigma^{(0)}$ according to Equation (12). These datasets can be used to improve the generality of the model trained on synthetic data to identify future crack evolutions more accurately. Specifically, this section presents a procedure based on domain adaptation to project the synthetic training dataset $\delta \bar{\mathbf{V}}$ onto a latent space with reduced dimensions, in which the distribution of the synthetic instances overlaps that of a set of real measurements $\delta \bar{\mathbf{v}}^{(c_r)}$ that triggered visual inspections. This process is carried out using TCA (S. J. Pan et al., 2011). Upon projecting the features onto the latent space, the model (i.e., the DNN used for early damage detection) can be refined to improve its accuracy for future predictions.

Domain adaptation is a feature-level strategy for transfer learning that allows transferring knowledge from a source



domain to a different yet related target domain through a convenient feature representation. This process consists of selecting a limited number of transfer components across domains, such that the features can be projected onto a latent space spanned by the selected transfer components, where their distributions overlap. TCA selects the transfer components in a reproducing kernel Hilbert space based on maximum mean discrepancy (MMD; S. J. Pan et al., 2011). Projected features can thus be employed to train a DNN with a smaller input layer. New instances from the target space can be used as an input of the DNN upon being projected onto the same latent space to predict a new conductivity distribution.

S. J. Pan et al. (2011) presented a TCA-based approach for domain adaptation, which encodes both labeled and unlabeled instances for selecting transfer components. This method operates by simultaneously addressing three optimization objectives, namely, (1) minimize the MMD between features distributions from the source and target domain in the latent space, (2) maximize the dependence of the projected features on the label information, and (3) preserving the local geometry of the data.

In this study, the source domain is represented by the synthetic dataset \mathcal{T} , obtained using the FE model (see Section 4). On the other hand, the target domain is that of real measurements, in which voltage differences are obtained by measurements at the electrodes of the conductive body, and the related conductivity variations are labeled during inspections.

Consider a matrix of real voltage measurements $\delta\bar{\mathbf{V}}^* = [\delta\bar{\mathbf{v}}^{(1)}, \dots, \delta\bar{\mathbf{v}}^{(C_r)}] \in \mathbb{R}^{K \times C_r}$ with the same structure as $\delta\bar{\mathbf{V}}$, where $\delta\bar{\mathbf{v}}^{(c_r)}$ are voltage measurements (herein addressed as “prior measurements”) that predicted new cracks in the past, triggering visual inspections. Here, C_r represents the number of inspections carried out at the time of the model refinement. It is worth noting that, in general, $C_r \ll C$. Similarly, consider a matrix of the relevant real labels generated during the inspections $\delta\bar{\Sigma}^* = [\delta\bar{\sigma}^{(1)}, \dots, \delta\bar{\sigma}^{(C_r)}] \in \mathbb{R}^{M \times C_r}$.

Consider also a further unlabeled voltage measurement $\delta\bar{\mathbf{v}}^{(C_r+1)}$ collected very recently (herein addressed as “current measurement”), for which we want to identify the corresponding conductivity distribution.

Let $\delta\bar{\mathbf{V}}^+$ be the union of the real and synthetic voltage datasets, such that $\delta\bar{\mathbf{V}}^+ = [\delta\bar{\mathbf{V}}, \delta\bar{\mathbf{V}}^*, \delta\bar{\mathbf{v}}^{(C_r+1)}] \in \mathbb{R}^{K \times \bar{C}}$, with $\bar{C} = C + C_r + 1$. Similarly, $\delta\bar{\Sigma}^+ = [\delta\bar{\Sigma}, \delta\bar{\Sigma}^*, \mathbf{0}] \in \mathbb{R}^{M \times \bar{C}}$ is the set of synthetic and real labels, with $\mathbf{0}$ representing a column vector of zeros. Thereby, an extended training set that includes the datasets of both domains can be defined as $\mathcal{T}^+ = \{\delta\bar{\mathbf{V}}^+, \delta\bar{\Sigma}^+\}$.

In general, due to the inherent differences between the source and target domains, the marginal probability distributions of the features are different, that is,

$P(\delta\bar{\mathbf{V}}) \neq P(\delta\bar{\mathbf{V}}^*)$. TCA assumes that a transformation τ exists such that $P(\tau(\delta\bar{\mathbf{V}})) \approx P(\tau(\delta\bar{\mathbf{V}}^*))$ and $P(\delta\bar{\Sigma}|\tau(\delta\bar{\mathbf{V}})) \approx P(\delta\bar{\Sigma}^*|\tau(\delta\bar{\mathbf{V}}^*))$. Instead of finding the nonlinear transformation directly, S. J. Pan et al. (2011) proposed a formulation to find a transformation matrix related to a kernel of the input data. This approach avoids the problems of local minima related to highly nonlinear transformations. Considering a linear kernel, let $\mathbf{K}_V = (\delta\bar{\mathbf{V}}^+)^T \delta\bar{\mathbf{V}}^+$ and $\mathbf{K}_\Sigma = (\delta\bar{\Sigma}^+)^T \delta\bar{\Sigma}^+$ be the kernel matrices of the voltage and conductivity data, respectively.

The MMD distance between the empirical means of the two domains can be minimized to ensure that the two distributions become more similar (Smola et al., 2007), that is, to extract domain-invariant features. This distance can be written as $\text{tr}(\mathbf{W}^T \mathbf{K}_V \mathbf{L} \mathbf{K}_V \mathbf{W})$, with $\text{tr}(\cdot)$ denoting the trace of its argument, $\mathbf{W} \in \mathbb{R}^{\bar{C} \times S}$ is the sought transformation matrix, and $\mathbf{L} \in \mathbb{R}^{\bar{C} \times \bar{C}}$ is a normalization matrix that accounts for the number of instances in the source and target domains, used to calculate the MMD:

$$[\mathbf{L}]_{ab} = \begin{cases} \frac{1}{C^2} & \text{if } a, b \leq C \\ \frac{1}{(C_r+1)^2} & \text{if } a, b > C \\ -\frac{1}{C+C_r} & \text{otherwise} \end{cases} \quad (15)$$

Therefore, optimization objective 1 consists of minimizing $\text{tr}(\mathbf{W}^T \mathbf{K}_V \mathbf{L} \mathbf{K}_V \mathbf{W})$, also considering a regularization term $\text{tr}(\mathbf{W}^T \mathbf{W})$ to control the complexity of \mathbf{W} .

Concerning optimization objective 2, let $\tilde{\mathbf{K}}_\Sigma$ be a matrix built to maximize the label dependence (Steinwart, 2001) and the variance on the source and target domains according to a weight parameter γ , such that

$$\tilde{\mathbf{K}}_\Sigma = \gamma \mathbf{K}_\Sigma + (1 - \gamma) \mathbf{I}_{\bar{C}} \quad (16)$$

with \mathbf{I}_n an identity matrix of size $n \times n$. It is worth noting that all the prior measurements are considered as labeled in this application, except the $(C_r + 1)^{\text{th}}$. However, also unlabeled data can be included in the first C_r instances by modifying \mathbf{K}_Σ suitably (i.e., by setting $[\mathbf{K}_\Sigma]_{ab} = 0$ if the relevant label was not measured). The influence of unlabeled data in TCA will be discussed in future studies.

In order to address optimization objective 3, two neighbor instances in the input space should still be neighbors in the latent space. To this aim, S. J. Pan et al. (2011) exploited the locality-preserving property of a manifold regularizer. Specifically, consider a matrix \mathbf{M} such that

$$[\mathbf{M}]_{ab} = \exp\left(-\frac{d_{ab}^2}{2\left(\sum_{a,b} d_{ab}\right)^2}\right) \quad (17)$$



if $\delta\bar{\mathbf{v}}^{(a)}$ is one of the k nearest neighbors of $\delta\bar{\mathbf{v}}^{(b)}$ (or vice versa), while $[\mathbf{M}]_{ab} = 0$ otherwise. In Equation (17), $\|\delta\bar{\mathbf{v}}^{(a)} - \delta\bar{\mathbf{v}}^{(b)}\|$ is the distance between two voltage instances. Let \mathcal{L} be the Laplacian matrix

$$\mathcal{L} = \tilde{\mathbf{M}} - \mathbf{M} \quad (18)$$

with

$$[\tilde{\mathbf{M}}]_{aa} = \sum_b [\mathbf{M}]_{ab} \quad (19)$$

The transformation matrix \mathbf{W} that projects the instances $\delta\bar{\mathbf{V}}^+$ onto a latent space that complies with the mentioned optimization criteria can thus be obtained by solving

$$\min_{\mathbf{W}} \left\{ \text{tr}(\mathbf{W}^T \mathbf{K}_V \mathbf{L} \mathbf{K}_V \mathbf{W}) + \mu \text{tr}(\mathbf{W}^T \mathbf{W}) + \frac{\lambda}{\bar{C}^2} \text{tr}(\mathbf{W}^T \mathbf{K}_V \mathcal{L} \mathbf{K}_V \mathbf{W}) \right\}$$

such that

$$\mathbf{W}^T \mathbf{K}_V \mathbf{H} \tilde{\mathbf{K}}_{\Sigma} \mathbf{H} \mathbf{K}_V \mathbf{W} = \mathbf{I}_S \quad (20)$$

where \mathbf{H} is a centering matrix defined as

$$\mathbf{H} = \mathbf{I}_{\bar{C}} - \bar{C}^{-1} \mathbf{1}_{\bar{C}} \quad (21)$$

with $\mathbf{1}_n$ representing a square matrix of ones of size $n \times n$, and $\mu > 0$, $\lambda \geq 0$ are tradeoff regularization and geometry parameters, respectively (S. J. Pan et al., 2011). Therefore, the first S eigenvectors of the matrix

$$\Psi = \left[\mathbf{K}_V \left(\mathbf{L} + \frac{\lambda}{\bar{C}^2} \mathcal{L} \right) \mathbf{K}_V + \mu \mathbf{I}_{\bar{C}} \right]^{-1} \mathbf{K}_V \mathbf{H} \tilde{\mathbf{K}}_{\Sigma} \mathbf{H} \mathbf{K}_V \quad (22)$$

constitute the columns of the transformation matrix $\mathbf{W} \in \mathbb{R}^{\bar{C} \times S}$. After obtaining the transformation matrix, the “updated” DNN can be trained using the synthetic labeled instances projected onto the latent space. Thereby, the new training dataset consists of $\mathcal{T}_p = \{\delta\bar{\mathbf{V}}_p, \delta\Sigma\}$, with $\bar{\mathbf{V}}_p$ representing the first C columns of $\mathbf{W}^T \mathbf{K}_V$. It is worth noting that the projected real instances are not used for training in this procedure to avoid overfitting. Also, the architecture of the updated DNN can be different from that of the original DNN, as the input layer is substantially smaller. In this study, the updated DNN has the same architecture as the preliminary DNN described in Section 4, with a lower number of neurons per layer (see Section 6.2 for more details).

The proposed transfer learning approach is schematized in Figure 3. First, a preliminary DNN is initialized using only synthetic data \mathcal{T} (a), which was shown effective for early damage detection. The trained network is then

employed in a monitoring process, consisting of periodically interrogating the conductive material and identifying cracks that constitute a set of prior measurements (b). When damage is detected, the relevant voltage measurement $\delta\bar{\mathbf{v}}^{(c_r)}$ is stored, and a visual inspection is planned, where the inspectors can annotate the crack location and generate a label $\delta\sigma^{(c_r)}$. Labeled instances are then used to generate \mathcal{T}^+ . When a sufficient number of instances from the target domain is available, the extended dataset can be employed to apply the TCA to improve the prediction of a new data instance $\delta\bar{\mathbf{v}}^{(C_r+1)}$, which is included in \mathcal{T}^+ without the label (c). The synthetic data projected onto the latent space can thus be used to train an updated DNN that will be employed to predict the conductivity distribution relevant to $\delta\bar{\mathbf{v}}^{(C_r+1)}$ and future interrogation data, according to the scheme of Figure 3b.

It is worth noting that DNNs have been employed in this study due to their well-acknowledged properties, including their high representational power and ease of use. However, the proposed transfer learning approach can be employed to extract domain-invariant features that can be used with any other machine learning method to reconstruct the conductivity map.

The size of the transformation matrix \mathbf{W} , that is, the number of most significant eigenvectors of the matrix Ψ is a parameter selected by the user. While many eigenvectors may include more information and thus lead to a more accurate conductivity reconstruction, the benefit of transfer learning is lost if this parameter is set too high, leading to overfitting noise, material, and geometry properties. On the other hand, underfitting with an excessively small size of \mathbf{W} would lead to the loss of information and low reconstruction accuracy. One criterion to select S consists of imposing a hard threshold to generate a transformation matrix \mathbf{W} with the eigenvectors associated with the largest S eigenvalues ω_s of Ψ , the sum of which is higher than a certain percentage η of the total sum of eigenvalues, that is,

$$\sum_{s=1}^S \omega_s > \eta \sum_{s=1}^{\bar{C}} \omega_s \quad (23)$$

6 | EXPERIMENTAL INVESTIGATION

This study presents the results obtained using four specimens fabricated at the ARMOR laboratory (University of California, San Diego). Specifically, two different paint formulations were used to investigate the benefit of information transfer among sensing films with different materials. The formulations are described in Section 6.1, as well as the specimen fabrication and the configuration of the FE model. Section 6.2 discusses the results obtained.

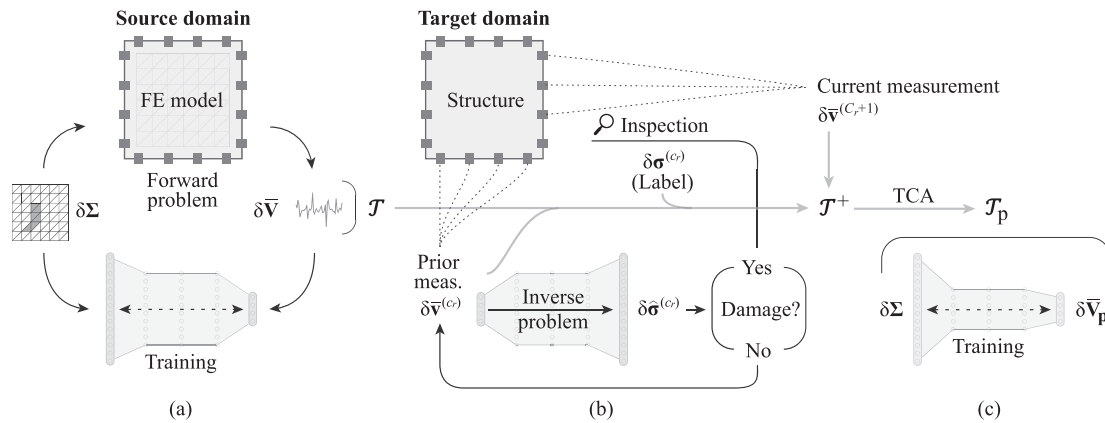


FIGURE 3 Monitoring phases: (a) initialization of the preliminary DNN, (b) construction of the extended training set using prior measurements, and (c) initialization of the DNN updated with transfer learning. FE, finite element; TCA, transfer component analysis.

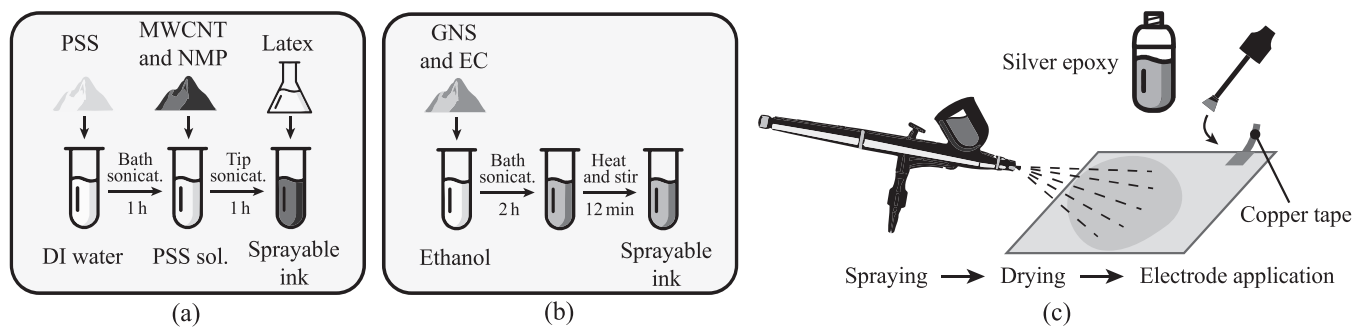


FIGURE 4 Specimen fabrication: (a) multi-walled carbon nanotubes (MWCNT)-based paint formulation, (b) graphene nanosheets (GNS)-based paint formulation, and (c) fabrication process. EC, ethyl cellulose; GNS, graphene nanosheets; MWCNT, multi-walled carbon nanotubes; NMP, N-methyl-2-pyrrolidinone; PSS, poly-(sodium 4-styrenesulfonate).

6.1 | Experimental setup

In the first paint formulation, 0.339 g of multi-walled carbon nanotubes (MWCNT; Mortensen et al., 2013) from NanoIntegris with an outer diameter of 8 nm were mixed with 0.806 g of N-methyl-2-pyrrolidinone (NMP) and 33.855 g of 2 wt.% poly-(sodium 4-styrenesulfonate) (PSS) solution (NMP and PSS provided by Sigma-Aldrich). The MWCNTs were dispersed by tip ultrasonication (more details on times and tip size are provided in Quqa et al., 2022). A sprayable ink was then obtained by adding a Latex solution (provided by Kynar Aquatec) and de-ionized water.

The second paint formulation is based on graphene nanosheets (GNS; Y. A. Lin et al., 2021; Lin et al., 2021b). GNS was first synthesized using water-assisted liquid-phase exfoliation (Manna et al., 2019) and then added to ethyl cellulose solution and subjected to bath sonication. The mixer was thus heated to 60°C and stirred for 12 min to generate a sprayable ink. The process to obtain the two formulations is schematized in Figure 4.

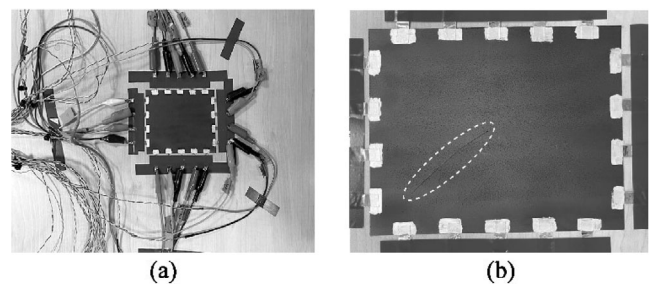


FIGURE 5 Experimental setup: (a) MWCNT-based specimen and interrogation setup and (b) example of induced crack.

The paints were manually sprayed onto four 108 × 132 mm² rectangular polyethylene terephthalate sheets (two for each sensing material) using a Paasche airbrush and air-dried for 12 h before use. In this study, specimens 1 and 2 were fabricated using the MWCNT-based formulation, while specimens 3 and 4 were fabricated using the GNS-based formulation. Copper tape strips were attached along the boundaries of the specimens (Figure 5) and used as electrodes (18 in total, in a 4 × 5 pattern). Silver epoxy (Ted

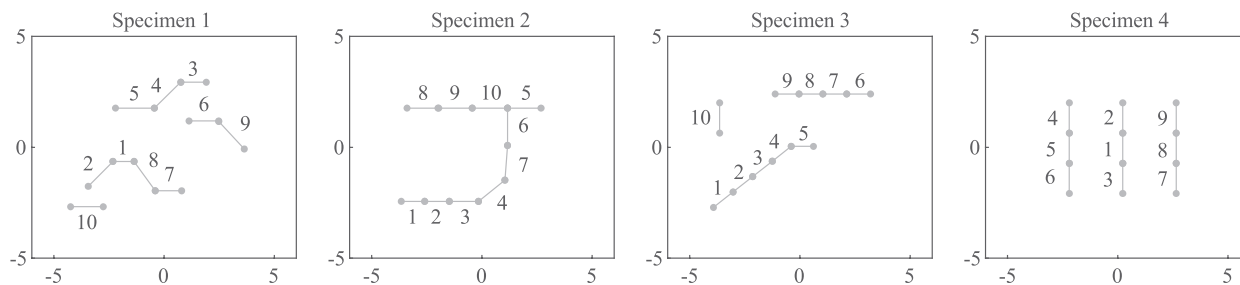


FIGURE 6 Crack sequences induced in the tested specimens; dimensions in cm.

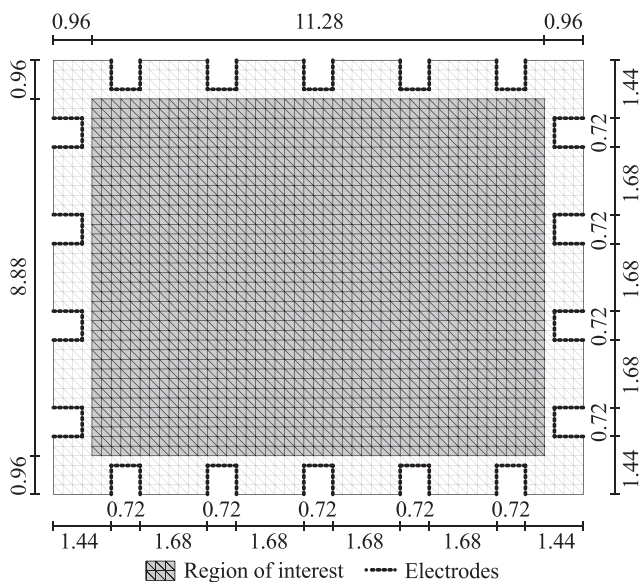


FIGURE 7 Scheme of the finite element (FE) model.

Pella) was applied over copper tapes to reduce the contact impedance.

A razor blade was employed to simulate cracks in the sensing film as shown in Figure 5. Specifically, the crack patterns reported in Figure 6 were applied, measuring voltage before and after each cut. A baseline measurement $\mathbf{v}^{(0)}$ was taken for each specimen before inducing damage. Then, after each crack, a new voltage measurement $\mathbf{v}^{(c_r)}$ was recorded and employed to calculate $\delta\bar{\mathbf{v}}^{(c_r)}$.

The specimen was fixed to the table using electrical insulating tape before cutting and interrogation. A data acquisition system was used to interrogate the specimens and collect voltage data. Specifically, an AC/DC (alternating current/direct current) generator (Keithley 6221) was employed to inject current using the adjacent interrogation pattern (Loyola et al., 2013), and a multifunctional switch with a digital multimeter (Keysight 34980A) was used to measure boundary voltage.

An FE model representing all the specimens was generated using a triangular mesh with the geometric properties described in Figure 7. The CEM was adopted for

boundary conditions as explained in Section 3. The initial conductivity of the material was set to 100 S/m. The set of C synthetic cracks mentioned in Section 4 was generated by simulating randomly distributed line-shaped regions with zero conductivity in the sensing surface. Specifically, a “crack line” was modeled as a random number (between 1 and 10) of connected segments with random lengths (max 2 cm each) and inclination. This line was positioned randomly within the surface of the model, in a selected region of interest with a size of $11.28 \times 8.88 \text{ cm}^2$, and the conductivity of the triangular elements of the mesh touching it was set to zero. In this study, the synthetic dataset includes 3000 labeled instances obtained in this way, that is, voltage data and the relevant conductivity distributions within the region of interest.

Both the preliminary and the updated DNNs were trained using the synthetic dataset described above. However, the preliminary DNN takes the normalized voltage measurements (Equation 11) in the input layer, while the updated DNN takes the features extracted through TCA.

As for the updated DNN, this study presents the results obtained in two monitoring scenarios. Both scenarios involve the set of 3000 synthetic labeled instances from the source domain generated by inducing random decrements in the conductivity of the FE model. Scenario 1 also involves eight labeled instances (i.e., prior measurements) from the target domain collected for specimens 1 and 2 (the first four crack propagation steps shown in Figure 6) to extend the training set. On the other hand, the second scenario involves 27 labeled instances from the target domain, that is, the eight already considered in scenario 1, plus all the 19 instances collected from specimens 3 and 4. Therefore, scenario 1 represents the case where the datasets are mainly collected from the monitored structures (i.e., prior information transfer). On the other hand, scenario 2 considers information transfer also among different structures in a population-level analysis. In this study, the difference between structures is given by the material formulation of the sensing film (see Section 6.1) and geometric dissimilarities due to fabrication errors.

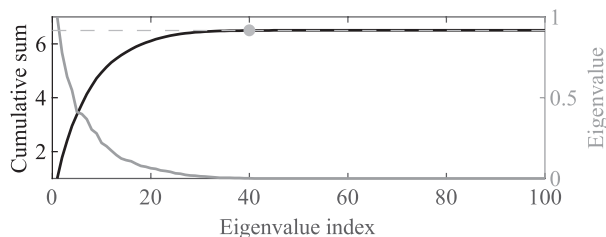


FIGURE 8 Selection of the latent space size.

The first step of the information transfer procedure consists of determining the size of the latent space. Figure 8 reports the first 100 eigenvalues of the matrix Ψ , normalized to the maximum value, obtained for scenario 1, in decreasing order of magnitude, as well as their cumulative sum. The base that spans the latent space was selected as the set of eigenvectors associated with the first S eigenvalues with a sum equal to at least 99.9% of the total sum of eigenvalues of Ψ . In this specific case, the resulting size of the latent space is 40. A size of 39 was obtained by repeating the calculation in scenario 2. Therefore, all the results presented in the following were obtained using $S = 40$.

6.2 | Discussion of the results

The transformation matrix \mathbf{W} was calculated for the two aforementioned scenarios. In scenario 1, the extended dataset was made of 3020 instances (i.e., including synthetic instances and prior measurements from specimens 1 and 2). In this case, only the labels of the first four crack patterns were included for both specimens. In scenario 2, the extended dataset was made of 3039 instances (i.e., also including prior measurements from specimens 3 and 4, together with their labels). Then, the extended dataset was projected onto the latent space ($\mathbb{R}^S, S = 40$) by calculating the projected matrix $\mathbf{W}^T \mathbf{K}_v$.

In general, the exact number of instances required in the target domain to successfully apply TCA can vary depending on the specific problem and the characteristics of the data. Since TCA minimizes the MMD between two distributions (in the source and target domains), the number of instances considered for each domain should be significant to describe the distribution they are extracted from. In the case of limited instances from the target domain, their significance can be assessed by evaluating the stability of their statistical moments. Figure 9 shows the first three statistical moments (i.e., mean, standard deviation, and kurtosis) of the norm of real voltage measurements for different sets of instances selected from the total set of 39 available experimental measurements, with increasing size. The analysis was repeated 10 times, considering a dif-

ferent set of random samples for each size of the considered set every time. The left-hand side of the figure reports the moments of each feature set as a function of the number of instances for every test conducted (10 different lines). The right-hand side of the figure shows the difference between consecutive points of the diagrams described above, in absolute value (gray lines), and their average (thick black line) calculated over the 10 different tests. These results show that the first statistical moments are quite stable when the number of considered instances is around 27. This means that the first statistical moments will likely not change much when adding more instances taken from the same distribution. Therefore, the set of samples considered in scenario 2 can represent the feature distribution in the target domain and allow for performing TCA properly. The statistical moments are more unstable when the number of considered instances is 8. This means that the conditions for performing TCA in scenario 1 may be suboptimal. However, it is worth noting that the MMD calculated between the synthetic and real raw voltage datasets was 0.457. On the other hand, after applying the TCA, the MMD between the sets of domain-invariant features extracted from synthetic and real datasets decreased to 0.240 in scenario 1 and 0.142 in scenario 2.

The higher similarity between real and synthetic instances is beneficial for generalization. An updated DNN was then trained using the synthetic part of the projected dataset \mathcal{T}_p and an architecture similar to the one described in Section 4. However, in this case, the hidden layers contained 256 neurons each, thus reducing the overall number of weights in the DNN by eight times. This value is similar to the reduction in the size of the input feature (i.e., S is about seven times smaller than K).

The updated network was fed with the projected real voltage measurements to predict the relevant distribution of conductivity variation. The results obtained using the preliminary DNN and the updated DNN in the two scenarios are reported in Figures 10 and 11 for each damage condition representing the crack propagation (C1–C10). In these figures, the grayscale contour plots represent the identified conductivity variations due to the induced cracks. Before and after each crack, a voltage measurement was taken. The relative conductivity variation for each crack step was first identified by setting the previous voltage measurement as a baseline, thus obtaining the plots on the right-hand side of the figure (last three columns). In order to make the identified cracks more easily observable, artifacts and conductivity variations due to material deformation have been removed by setting a threshold equal to half of the maximum conductivity reduction identified at each step, below which any other conductivity variations were canceled. This application is only focused on crack identification, which entails total conductivity loss.

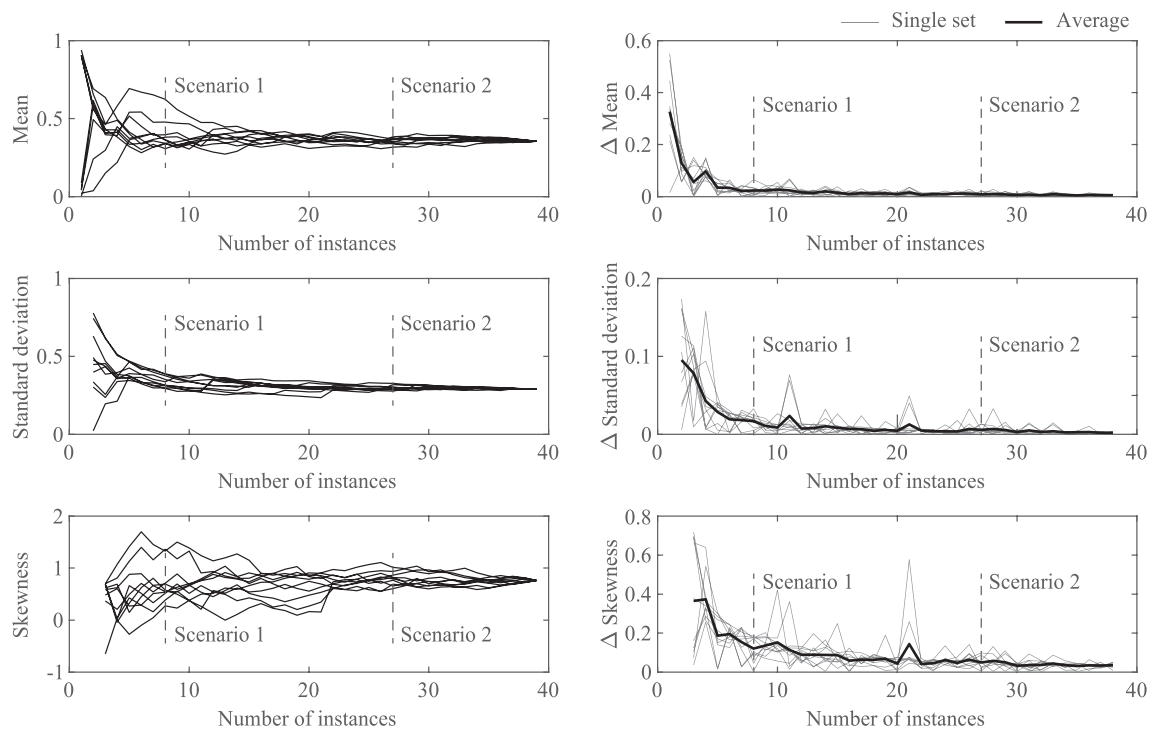


FIGURE 9 Statistical moments of the norm of real voltage measurements.

Therefore, only high conductivity variations are interpreted as cracks. Since the input voltage was normalized (as shown in Equation 11), the identified conductivity variation is dimensionless.

In the left-hand part of Figures 10 and 11, the cumulative conductivity variation is also represented as the sum of relative variations identified before each inspection. Relative and cumulative plots have different color scaling to improve representation clarity. A dotted hatch is used when the conductivity distribution exceeds the maximum representation scale. In these figures, the thick black lines represent the reference crack patterns, that is, those reported in Figure 6. Moreover, the “+” symbols depicted on the conductivity variation plots represent the centroids of identified cracks (i.e., the weighted means of the identified conductivity variations). The Euclidean distance between these centroids and the center of progressively induced cracks is used in this study as a performance index of the identification method. Since specimens 3 and 4 have been used for training in scenario 2, Figures 10 and 11 only present the results for specimens 1 and 2.

The gain obtained from applying the proposed approach can be appraised by comparing the conductivity reconstructions obtained through the preliminary and the updated DNNs. In general, the preliminary DNN provides more concentrated conductivity variations than the updated DNNs for the first crack patterns. However, the reconstruction accuracy suddenly drops for more complex patterns, that is, after C4 for both specimens, failing

in damage localization. Indeed, in more complex damage patterns, the relative conductivity variation identified by the preliminary DNN mainly consists of small regions distributed throughout the sensing surface. On the other hand, the relative conductivity distributions predicted using projected data typically present concentrated low-conductivity regions close to the location of reference cracks. Moreover, the DNN used in scenario 2 typically provides better localization results with fewer artifacts (e.g., see C9 in specimen 1 and C7 in specimen 2).

Also, the total variation (TV) algorithm (Holder, 2004) was employed to have a reference comparison with a “standard” literature method. Figure 12 shows the results obtained using the TV method for the two analyzed specimens. More details on the application of this method to difference voltage data can be found in (Quqa et al., 2022). In this study, a regularization coefficient equal to 10^{-6} was employed. The results obtained using the TV method generally have better localization performance in the first stages of cracking, similar to those of the preliminary DNN. However, crack localization accuracy tends to reduce for complex crack patterns, that is, after C5. In the last damage cases, several artifacts populate the identified conductivity distribution.

The Euclidean distance was calculated between the centroids of reference and identified progressive cracks (i.e., the relative conductivity variation) for all analyzed cases (herein called “inspections”) as a performance indicator for crack localization. Figure 13 shows the distances for

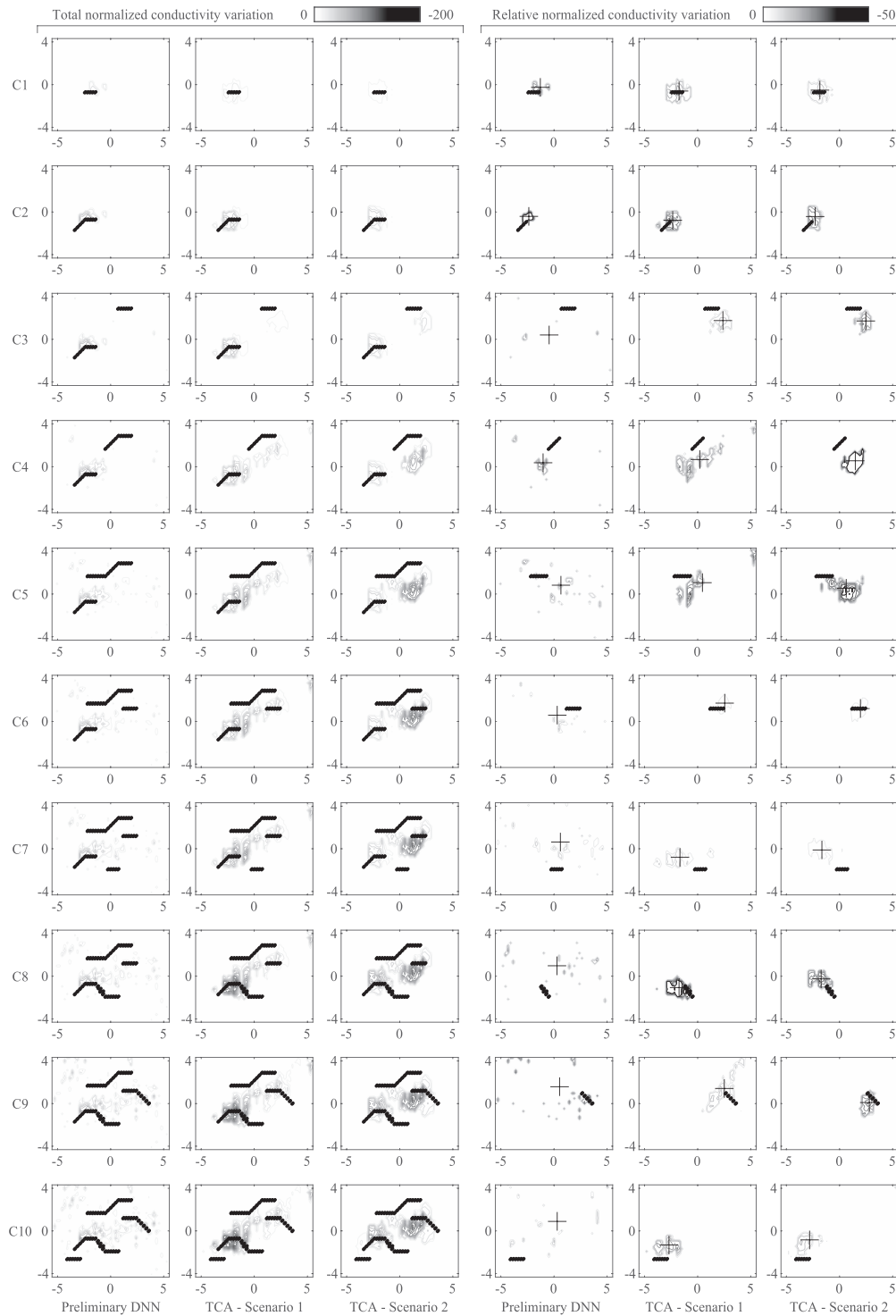


FIGURE 10 Experimental results for specimen 1. Left: total normalized conductivity variation; right: relative normalized conductivity variations. The gray contour depicts the identified conductivity, + symbols represent their centroids, and thick black lines are the reference cracks.

the TV method, the preliminary DNN, and the updated DNNs using TCA in both scenarios. A linear regression of the distance values over time was also calculated (thick gray lines). Generally, while the TV method and the preliminary DNN provide results with an increasing distance

over time (denoting decreasing performance), the TCA has an almost flat (and lower) trend, especially in scenario 2. This confirms that using transfer learning is beneficial for improving the performance of crack identification for complex crack patterns.



FIGURE 11 Experimental results for specimen 2. Left: total normalized conductivity variation; right: relative normalized conductivity variations. The gray contour depicts the identified conductivity, + symbols represent their centroids, and thick black lines are the reference cracks.

7 | CONCLUSION

This study investigated the possibility of improving the performance of DNNs for conductivity reconstruction in

the inverse EIT problem using transfer learning. A new strategy was proposed for including annotations taken by operators during visual inspections through a domain adaptation process based on TCA.

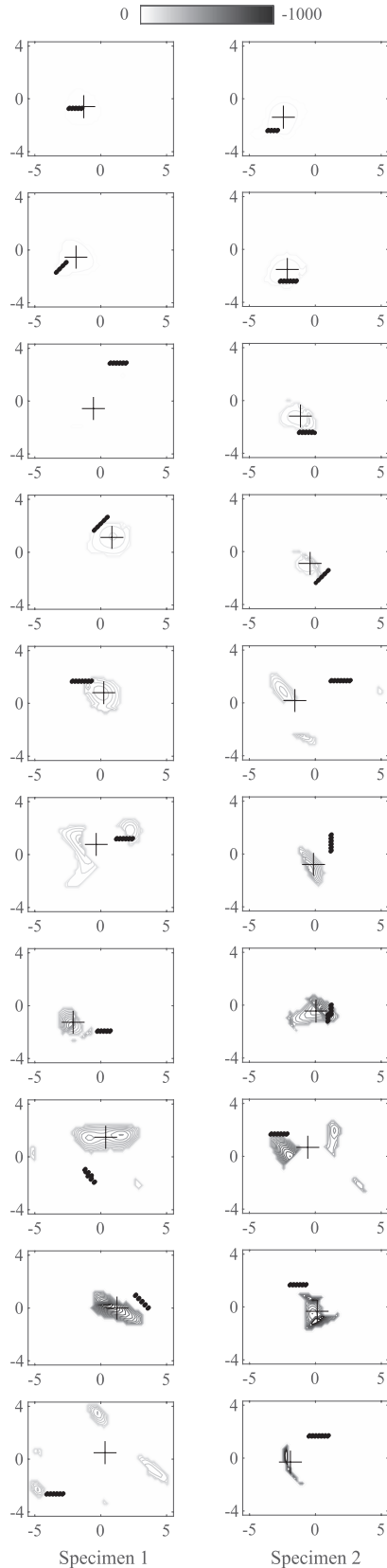


FIGURE 12 Relative normalized conductivity variation identified using the total variation (TV) method.

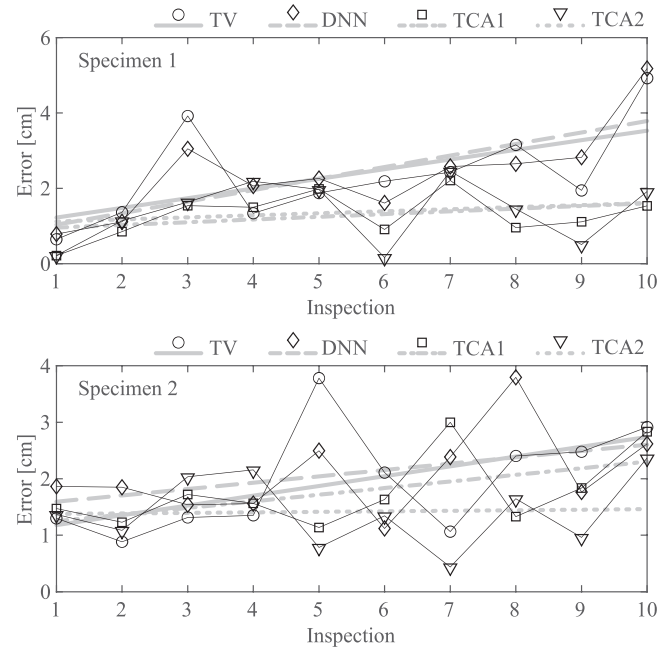


FIGURE 13 Euclidean distance between the identified and reference cracks. Thin black lines indicate the performance of each inspection; Thick gray lines indicate the linear regression. TCA, transfer component analysis.

The method was tested for crack identification using sensing films obtained by depositing a sprayable conductive ink onto the monitored element. Two different scenarios were tested, one including only information collected at early damage states of the monitored structures and one exploiting information transfer at a population level.

After applying domain adaptation, real and synthetic voltage measurements showed a higher level of similarity, thus demonstrating the effectiveness of the procedure. The higher performance of the updated neural networks (trained using the projected data) was also proven by comparing the conductivity reconstructions obtained through regression. The Euclidean distance between the centroids of reference and identified cracks was used as a performance index for damage localization. Predicting crack location based on the preliminary DNN provided results with an accuracy similar to that of the TV method, a traditional approach for solving the inverse EIT problem. Specifically, the first cracks were identified with good accuracy. Identification performance diminished with the increasing complexity of the crack pattern. On the other hand, including early damage information in the training process through transfer learning substantially improved the ability of the neural network to identify advanced damage states. Moreover, information collected on specimens with similar geometry and different



material further increased the performance of the machine learning approach, giving a new value to the information collected during other inspection campaigns. Improvements in crack identification accuracy are fundamental in the perspective of SHM of civil infrastructure.

ACKNOWLEDGMENTS

This research was supported by the US Army Corp of Engineers, Engineer Research and Development Center (principal investigator: Prof. Michael D. Todd), under Cooperative Research Agreements W912HZ-17-2-0024 and W9132T-22-2-20014. It was also supported by the European Union's Horizon 2020 research and innovation programme under the Marie Skłodowska-Curie grant agreement No. 777822.

ORCID

Said Quqa <https://orcid.org/0000-0001-6388-370X>

Luca Landi <https://orcid.org/0000-0001-7259-1186>

Kenneth J. Loh <https://orcid.org/0000-0003-1448-6251>

REFERENCES

- Borcea, L. (2002). Electrical impedance tomography. *Inverse Problems*, 18(6), R99–R136.
- Bull, L. A., Gardner, P. A., Gosliga, J., Rogers, T. J., Dervilis, N., Cross, E. J., Papatheou, E., Maguire, A. E., Campos, C., & Worden, K. (2021). Foundations of population-based SHM, Part I: Homogeneous populations and forms. *Mechanical Systems and Signal Processing*, 148, 107141.
- Calderón, A. P. (2006). On an inverse boundary value problem. *Computational & Applied Mathematics*, 25(2–3).
- Capps, M., & Mueller, J. L. (2020). Reconstruction of organ boundaries with deep learning in the D-bar method for electrical impedance tomography. *IEEE Transactions on Biomedical Engineering*, 68(3), 1–1.
- Chen, J., Lu, W., & Lou, J. (2022). Automatic concrete defect detection and reconstruction by aligning aerial images onto semantic-rich building information model. *Computer-Aided Civil and Infrastructure Engineering*, 38(8), 1079–1098.
- Chen, L., Gallet, A., Huang, S.-S., Liu, D., & Smyl, D. (2022). Probabilistic cracking prediction via deep learned electrical tomography. *Structural Health Monitoring*, 21(4), 1574–1589.
- Chen, L., Hassan, H., Tallman, T. N., Huang, S.-S., & Smyl, D. (2022). Predicting strain and stress fields in self-sensing nanocomposites using deep learned electrical tomography. *Smart Materials and Structures*, 31(4), 045024.
- Chen, Z., Yang, Y., & Bagnaninchi, P. O. (2021). Hybrid learning-based cell aggregate imaging with miniature electrical impedance tomography. *IEEE Transactions on Instrumentation and Measurement*, 70, 70.
- Chun, P., Yamane, T., & Maemura, Y. (2022). A deep learning-based image captioning method to automatically generate comprehensive explanations of bridge damage. *Computer-Aided Civil and Infrastructure Engineering*, 37(11), 1387–1401.
- Clevert, D.-A., Unterthiner, T., & Hochreiter, S. (2015). Fast and accurate deep network learning by exponential linear units (ELUs). arXiv:1511.07289v5.
- Deng, J., Lu, Y., & Lee, V. C. (2020). Concrete crack detection with handwriting script interferences using faster region-based convolutional neural network. *Computer-Aided Civil and Infrastructure Engineering*, 35(4), 373–388.
- Gupta, S., Gonzalez, J. G., & Loh, K. J. (2017). Self-sensing concrete enabled by nano-engineered cement-aggregate interfaces. *Structural Health Monitoring*, 16(3), 309–323.
- Gupta, S., Vella, G., Yu, I. N., Loh, C. H., Chiang, W. H., & Loh, K. J. (2020). Graphene sensing meshes for densely distributed strain field monitoring. *Structural Health Monitoring*, 19(5), 1323–1339.
- Hallaji, M., & Pour-Ghaz, M. (2014). A new sensing skin for qualitative damage detection in concrete elements: Rapid difference imaging with electrical resistance tomography. *NDT & E International*, 68, 13–21.
- Hallaji, M., Seppänen, A., & Pour-Ghaz, M. (2014). Electrical impedance tomography-based sensing skin for quantitative imaging of damage in concrete. *Smart Materials and Structures*, 23(8).
- Harikumar, R., Prabu, R., & Raghavan, S. (2013). Electrical impedance tomography (EIT) and its medical applications: A review. *International Journal of Soft Computing and Engineering (IJSCE)*, 3(4), 193–198.
- Holder, D. (2004). *Electrical impedance tomography—Methods, history and applications*. CRC Press.
- Hou, T. C., Loh, K. J., & Lynch, J. P. (2007). Spatial conductivity mapping of carbon nanotube composite thin films by electrical impedance tomography for sensing applications. *Nanotechnology*, 18(31), 315501.
- Hu, N., Karube, Y., Yan, C., Masuda, Z., & Fukunaga, H. (2008). Tunneling effect in a polymer/carbon nanotube nanocomposite strain sensor. *Acta Materialia*, 56(13), 2929–2936.
- Jauhiainen, J., Pour-Ghaz, M., Valkonen, T., & Seppänen, A. (2021). Nonplanar sensing skins for structural health monitoring based on electrical resistance tomography. *Computer-Aided Civil and Infrastructure Engineering*, 36(12), 1488–1507.
- Jeon, D., Kim, M. K., Jeong, Y., Oh, J. E., Moon, J., Kim, D. J., & Yoon, S. (2022). High-accuracy rebar position detection using deep learning-based frequency-difference electrical resistance tomography. *Automation in Construction*, 135, 104116.
- Li, S., Shu, Y., Lin, Y.-A., Zhao, Y., Yeh, Y.-J., Chiang, W.-H., & Loh, K. J. (2022). Distributed strain monitoring using nanocomposite paint sensing meshes. *Sensors*, 22(3), 812.
- Li, S., Zhao, X., & Zhou, G. (2019). Automatic pixel-level multiple damage detection of concrete structure using fully convolutional network. *Computer-Aided Civil and Infrastructure Engineering*, 34(7), 616–634.
- Lin, Y., Nie, Z., & Ma, H. (2022). Dynamics-based cross-domain structural damage detection through deep transfer learning. *Computer-Aided Civil and Infrastructure Engineering*, 37(1), 24–54.
- Lin, Y.-A., schraefel, m. c., Chiang, W.-H., & Loh, K. J. (2021). Wearable nanocomposite kinesiology tape for distributed muscle engagement monitoring. *MRS Advances*, 6(1), 6–13. <https://doi.org/10.1557/s43580-021-00005-4>
- Lin, Y. A., Zhao, Y., Wang, L., Park, Y., Yeh, Y., Chiang, W., & Loh, K. J. (2021). Graphene K-tape meshes for densely distributed human motion monitoring. *Advanced Materials Technologies*, 6(1), 2000861.
- Lin, Z., Guo, R., Zhang, K., Li, M., Yang, F., Xu And, S., & Abubakar, A. (2020). Neural network-based supervised descent method for



- 2D electrical impedance tomography. *Physiological Measurement*, 41(7).
- Liu, Y., Nie, X., Fan, J., & Liu, X. (2020). Image-based crack assessment of bridge piers using unmanned aerial vehicles and three-dimensional scene reconstruction. *Computer-Aided Civil and Infrastructure Engineering*, 35(5), 511–529.
- Loh, K. J., Hou, T. C., Lynch, J. P., & Kotov, N. A. (2009). Carbon nanotube sensing skins for spatial strain and impact damage identification. *Journal of Nondestructive Evaluation*, 28(1), 9–25.
- Loh, K. J., Kim, J., Lynch, J. P., Kam, N. W. S., & Kotov, N. A. (2007). Multifunctional layer-by-layer carbon nanotube–polyelectrolyte thin films for strain and corrosion sensing. *Smart Materials and Structures*, 16(2), 429–438.
- Loyola, B. R., La Saponara, V., & Loh, K. J. (2010). In situ strain monitoring of fiber-reinforced polymers using embedded piezoresistive nanocomposites. *Journal of Materials Science*, 45(24), 6786–6798.
- Loyola, B. R., La Saponara, V., Loh, K. J., Briggs, T. M., O'Bryan, G., & Skinner, J. L. (2013). Spatial sensing using electrical impedance tomography. *IEEE Sensors Journal*, 13(6), 2357–2367.
- Manna, K., Wang, L., Loh, K. J., & Chiang, W. (2019). Printed strain sensors using graphene nanosheets prepared by water-assisted liquid phase exfoliation. *Advanced Materials Interfaces*, 6(9), 1900034.
- Meoni, A., D'Alessandro, A., & Ubertini, F. (2020). Characterization of the strain-sensing behavior of smart bricks: A new theoretical model and its application for monitoring of masonry structural elements. *Construction and Building Materials*, 250, 118907.
- Mortensen, L. P., Ryu, D. H., Zhao, Y. J., & Loh, K. J. (2013). Rapid assembly of multifunctional thin film sensors for wind turbine blade monitoring. *Key Engineering Materials*, 569–570, 515–522.
- Nayyeri, F., Hou, L., Zhou, J., & Guan, H. (2019). Foreground–background separation technique for crack detection. *Computer-Aided Civil and Infrastructure Engineering*, 34(6), 457–470.
- Pan, S. J., Tsang, I. W., Kwok, J. T., & Yang, Q. (2011). Domain adaptation via transfer component analysis. *IEEE Transactions on Neural Networks*, 22(2), 199–210.
- Pan, Y., & Zhang, L. (2022). Dual attention deep learning network for automatic steel surface defect segmentation. *Computer-Aided Civil and Infrastructure Engineering*, 37(11), 1468–1487.
- Quqa, S., Li, S., Shu, Y., Landi, L., & Loh, K. J. (2023). Crack identification using smart paint and machine learning. *Structural Health Monitoring*, 147592172311678. <https://doi.org/10.1177/14759217231167823>
- Quqa, S., Shu, Y., Li, S., & Loh, K. J. (2022). Pressure mapping using nanocomposite-enhanced foam and machine learning. *Frontiers in Materials*, 9.
- Rafiei, M. H., & Adeli, H. (2017). A novel machine learning-based algorithm to detect damage in high-rise building structures. *The Structural Design of Tall and Special Buildings*, 26(18), e1400.
- Seppänen, A., Hallaji, M., & Pour-Ghaz, M. (2017). A functionally layered sensing skin for the detection of corrosive elements and cracking. *Structural Health Monitoring*, 16(2), 215–224.
- Smola, A., Gretton, A., Song, L., & Schölkopf, B. (2007). A Hilbert space embedding for distributions. In M. Hutter, R. A. Servadio, & E. Takimoto (Eds.), *Algorithmic learning theory* (pp. 13–31). Springer.
- Soleimani-Babakamali, M. H., Sepasdar, R., Nasrollahzadeh, K., Lourentzou, I., & Sarlo, R. (2022). Toward a general unsupervised novelty detection framework in structural health monitoring. *Computer-Aided Civil and Infrastructure Engineering*, 37(9), 1128–1145.
- Steinwart, I. (2001). On the influence of the kernel on the consistency of support vector machines. *Journal of Machine Learning Research*, 2, 67–93.
- Tallman, T. N., Gungor, S., Wang, K. W., & Bakis, C. E. (2014). Damage detection and conductivity evolution in carbon nanofiber epoxy via electrical impedance tomography. *Smart Materials and Structures*, 23(4).
- Tallman, T. N., & Smyl, D. J. (2020). Structural health and condition monitoring via electrical impedance tomography in self-sensing materials: A review. *Smart Materials and Structures*, 29(12), 123001.
- Wu, L., Lin, X., Chen, Z., Lin, P., & Cheng, S. (2021). Surface crack detection based on image stitching and transfer learning with pretrained convolutional neural network. *Structural Control and Health Monitoring*, 28(8).
- Xue, Q., & Zhang, K. (2022). IPDC network-based image reconstruction for damage detection of CFRP with electrical impedance tomography. *IEEE Sensors Journal*, 22(13), 13244–13250.
- Zhang, C., Chang, C., & Jamshidi, M. (2020). Concrete bridge surface damage detection using a single-stage detector. *Computer-Aided Civil and Infrastructure Engineering*, 35(4), 389–409.
- Zhang, Y., & Yuen, K. (2021). Crack detection using fusion features-based broad learning system and image processing. *Computer-Aided Civil and Infrastructure Engineering*, 36(12), 1568–1584.
- Zheng, Y., Gao, Y., Lu, S., & Mosalam, K. M. (2022). Multistage semisupervised active learning framework for crack identification, segmentation, and measurement of bridges. *Computer-Aided Civil and Infrastructure Engineering*, 37(9), 1089–1108.

How to cite this article: Quqa, S., Landi, L., & Loh, K. J. (2023). Crack identification using electrical impedance tomography and transfer learning. *Computer-Aided Civil and Infrastructure Engineering*, 38, 2426–2442. <https://doi.org/10.1111/mice.13043>